Experimental Robotics I," eds. Hayward, V. and Khatib O.,
Springer - Verlag Berlin
Heidelberg 1990.

Design and Development of Torque-Controlled Joints

Dieter Vischer and Oussama Khatib

Robotics Laboratory
Computer Science Department
Stanford University

Abstract

This paper discusses the effect of basic manipulator characteristics upon the implementation of high performance joint torque control. Two manipulators with very different characteristics (high and low gear ratios) are used in this analysis: The PUMA 560 manipulator and ARTISAN, a ten degree-of-freedom manipulator currently under development at Stanford. The experimental results obtained with a prototype link of ARTISAN are presented and compared to those previously obtained with the PUMA. This paper also describes conceptually a new type of torque sensor, developed during the course of this project. With this new sensor, using inductive contactless transducers, torques are evaluated by distance measurements of deflections in the sensor's structure. The new sensor provides a substantial increase in accuracy over conventional strain gauge sensors, achieves higher mechanical robustness, and presents lower sensitivity to electrical noise.

1 Introduction

The work reported in this paper is part of a larger research effort concerned with the development of a high-performance, force-controlled, ten degree-of-freedom manipulator, ARTISAN, currently under development at Stanford University (Roth et al. 1988). Force control has emerged as one of the basic means to extend robot capabilities in performing advanced tasks in complex environments. A prerequisite to force control implementation is the manipulator's ability to achieve precise control of joint torques. This ability, however, is considerably restricted by the nonlinearities and friction inherent in the actuator-transmission systems generally found in industrial robots.
The list of desirable properties of a force controlled manipulator includes: high backdrivability, low friction, minimal effects of ripple torques and dynamic forces, high ratio of force capacity to force accuracy (Townsend 1988), little backlash, and negligible distributed elasticities (Colgate and Hogan 1989, Eppinger 1986 and 1987).
While avoiding transmission nonlinearities, direct drive manipulators become increasingly massive and bulky with increases in the number of degrees of freedom. The solution

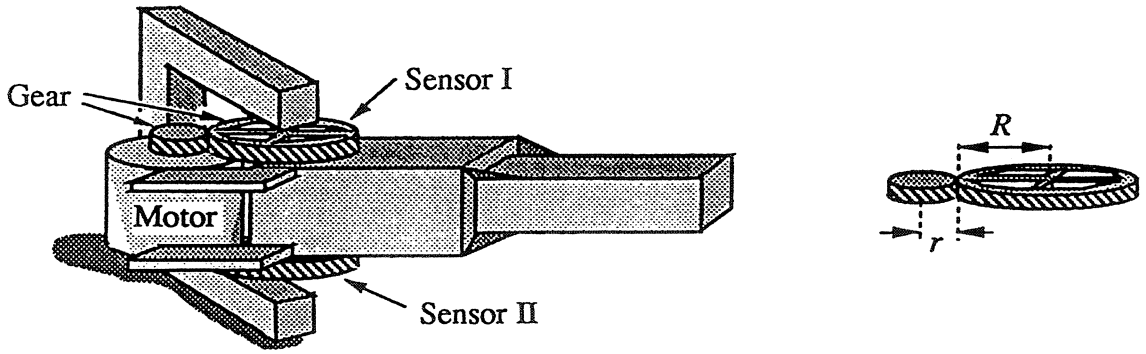

Figure 1: Prototype Link

we have adopted for the actuation of ARTISAN has been to use brushless (permanent magnet) motors and a single stage, low gear reduction (evoloid) system with torque sensing. Joint torque feedback is aimed at reducing friction and transmission effects, thus providing high performance joint torque control. The goal is to design, for each joint, an independent, high-bandwidth, robust torque servo controller.
The first part of the following description deals with the basic characteristics of torque controlled joints, where high-geared and low-geared manipulators will be compared. The second part focuses on the design and development of the new torque sensor.

2 Torque Control

Joint torque performance depends strongly on the gains achievable by the controller. A better understanding of the limitations placed on these gains has been one of the major objectives in our experiments with the prototype link.

2.1 Prototype Link

The prototype link for ARTISAN is shown in Figure 1. It uses a brushless dc motor, mounted at the base of the link in order to counterbalance the link's mass. The motor torque is transmitted in parallel through two single-stage low gear-reduction transmissions. The torque sensor is integrated with the gear. A shaft encoder is located on the motor axis to measure the relative position between the link and the motor. The parameters of the prototype link are given in Table 1.
The equations of motion of the link involve additional dynamic forces resulting from the rotation of the motor relative to the link. During a full revolution of the link, the motor makes $N+1$ turns

$$T_m - \frac{T_s}{N} = J_m(\ddot{\theta}_m + \ddot{\theta}_l) + d_m\dot{\theta}_m; \quad (1)$$

$$T_s(1+\frac{1}{N}) - T_m = (\tilde{J}_l + m(R+r)^2)\ddot{\theta}_l + d_l\dot{\theta}_l - d_m\dot{\theta}_m. \quad (2)$$

Table 1: Link Parameters

N	Gear Ratio	m	Motor Mass
$\tilde{J}_l$	Link Inertia	J_m	Motor Inertia
d_l	Link Friction	d_m	Motor Friction
T_s	Sensor Torque	T_m	Motor Torque
θ_l	Link Angle	θ_m	Motor Angle

The torque sensor can be modeled as a linear spring, where k_s is the total stiffness of sensors I and II

$$T_s = k_s\theta_s; \tag{3}$$

and θ_s is the angle of sensor deflection

$$\theta_s = \frac{\theta_m}{N} - \theta_l. \tag{4}$$

2.2 Torque Transfer Function

The transfer function of motor torque T_m to sensed torque T_s (which corresponds to the joint torque) can be obtained from equations (1), (2), (3) and (4) as

$$\frac{T_s}{T_m} = \frac{(\frac{k_s}{NJ_m} + \frac{k_s}{NJ_l} + \frac{k_s}{J_l})s + \frac{d_l k_s}{NJ_m J_l}}{s^3 + (\frac{d_m}{J_m} + \frac{d_l}{J_l} + \frac{d_m}{J_l})s^2 + (\frac{k_s}{N^2 J_m} + \frac{k_s}{J_l} + \frac{2k_s}{NJ_l} + \frac{k_s}{N^2 J_l} + \frac{d_l d_m}{J_m J_l})s + \frac{k_s}{J_m J_l}(\frac{d_l}{N^2} + d_m)}; \tag{5}$$

where

$$J_l = m(R+r)^2 + \tilde{J}_l.$$

Experimental frequency and step responses have shown the system to have a dominant second order behavior with weak damping. Thus, a first approximation of the transfer function can be obtained by neglecting the damping terms d_m and d_l. By setting $(d_m = d_l = 0)$, equation (5) is reduced to

$$\frac{T_s}{NT_m} = \frac{k_0\omega_0^2}{s^2 + \omega_0^2} \quad \begin{cases} k_0 = \frac{(N+1)J_m + J_l}{(N+1)^2 J_m + J_l} \leq 1; \\ \omega_0^2 = k_s \frac{(N+1)^2 J_m + J_l}{N^2 J_m J_l}; \end{cases} \tag{6}$$

where k_0 is the open-loop gain and $\omega_0/2\pi$ is the open-loop frequency, f_0. Observing that $N \gg 1$ and $J_l \gg NJ_m$, the parameters k_0 and ω_0 can be further simplified to

$$k_0 = \frac{1}{1 + \frac{N^2 J_m}{J_l}}; \tag{7}$$

$$\omega_0^2 = k_s(\frac{1}{J_l} + \frac{1}{N^2 J_m}). \tag{8}$$

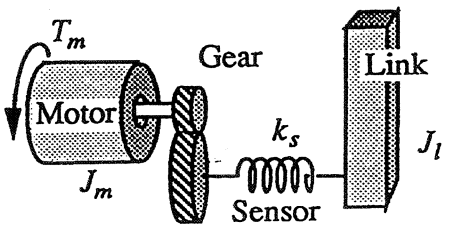

Figure 2: Approximated Model

Equations (7) and (8) correspond to a link with an inertia J_l driven by a motor, which is fixed in the inertial frame, as shown in Figure 2.
The transfer function for the constrained link can be found from equation (5) by letting J_l go to infinity

$$\frac{T_s}{NT_m} = \frac{k_0\omega_0^2}{s^2 + 2\xi_0\omega_0 s + \omega_0^2}; \quad \text{with} \quad k_0 = 1; \quad \xi_0 = \frac{d_m}{2\omega_0 J_m}; \quad \text{and} \quad \omega_0^2 = \frac{k_s}{N^2 J_m}. \tag{9}$$

2.3 Disturbances

Static friction (Coulomb friction), dynamic friction, and motor ripple torques can be regarded as disturbance torques acting on the motor. The sensed torque is also effected by other disturbances originating at the link (friction in the gears and dynamic forces resulting from the action of other links or from the link interaction with the environment).
Some of these effects can be modeled, identified, and compensated for in the control algorithm. Armstrong (1988) has shown the effectiveness of feedforward compensations using look up tables. Our goal is to couple feedforward compensations with joint torque feedback to provide high reduction of unmodeled disturbances and robustness to model errors. Unknown disturbances and model errors can be grouped into two classes:

- T_{d1} : the sum of disturbances originating at the motor;
- T_{d2} : the sum of disturbances acting at the link.

The transfer function (with $d_l = d_m = 0$) then becomes

$$T_s = \frac{k_0\omega_0^2}{s^2 + \omega_0^2}(NT_m + T_d); \quad \text{with} \quad T_d = NT_{d1} + \frac{N^2 J_m}{J_l} T_{d2}. \tag{10}$$

Equation (10) describes the influence of disturbances on the open-loop system (see Figure 3). One of the advantages of low geared robots such as ARTISAN is that their open-loop characteristics, k_0 and f_0, are less sensitive to changes in the link inertia, J_l. In addition, sensed torques are less sensitive to the disturbance torque, T_{d2}, acting at the link (equation 10). This is illustrated in the following two examples.

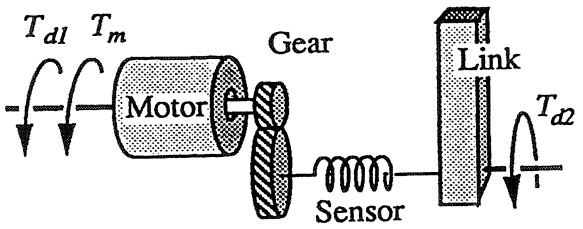

Figure 3: Disturbance Torques

Table 2: Prototype and PUMA Parameters

	Prototype	PUMA
Gear Ratio, N	6	53.7
$\frac{N^2 J_m}{J_l}$	0.12	2.5
Motor Inertia, J_m	0.000755 kg m^2	0.000288 kg m^2
Link Inertia, J_l	0.23 kg m^2	0.336 kg m^2
Spring Constant, k_s	452000 Nm/rad	16000 Nm/rad

2.4 Examples

Pfeffer, Khatib, and Hake (1986) have developed a joint torque sensory feedback controller for the third link of a PUMA 560 manipulator. The PUMA 560 is an example of a relatively high geared manipulator. Here, it is used to provide a basis for comparison with the low geared prototype link of ARTISAN.

The relevant parameters for the ARTISAN prototype and the PUMA are shown in Table 2. The open-loop characteristic for the two examples, obtained from equations (6), (9), and (10), are summarized in Table 3.

The data in Table 3 confirms the advantages of low over high gear-ratio manipulators discussed above. The dominance of a second order behavior in the dynamics of the prototype link has been confirmed by experimental open-loop step responses (see Figure 9). These experiments have shown the resonant frequency to be at 230 Hz for both the

Table 3: Open-Loop Characteristics

		Prototype	PUMA
Open-Loop Gain, k_0	Link Free	0.88	0.29
	Link Fixed	1	1
Open-Loop Frequency, f_0	Link Free	699 Hz	41 Hz
	Link Fixed	650 Hz	22 Hz
Disturbance (Link Free)	$\frac{T_s}{T_{d1}}\|_{s=0}$	5.28	15.6
	$\frac{T_s}{T_{d2}}\|_{s=0}$	0.18	0.73

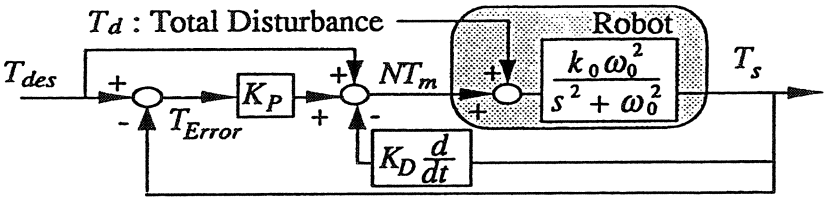

Figure 4: PD Controller

free and constrained link cases. This value is significantly lower than the frequencies of 699 Hz and 650 Hz estimated using the model. This discrepancy is due to significant flexibility in the transmission system that was neglected in the model. In effect, the experimental data have shown the overall stiffness to be much lower than the stiffness of the sensor.

2.5 Lead Controllers

Disturbance rejection and robustness characteristics of lead-type controllers can best be analyzed by using a simple PD controller. The control law (see Figure 4) is

$$NT_m = T_{des} - K_P(T_s - T_{des}) - K_D\dot{T}_s; \tag{11}$$

where K_P and K_D are the proportional and derivative feedback gains, respectively. The input feedforward allows to reduce static errors.

The closed-loop transfer function can be obtained from equations (10) and (11) as

$$T_s = \frac{k_c\omega_c^2}{s^2+2\xi_c\omega_c s+\omega_c^2}(T_{des}+\frac{T_d}{K_P+1}); \tag{12}$$

where the closed-loop gain k_c, damping ξ_c and frequency f_c are

$$k_c = \frac{1}{1+\frac{J_m^*}{J_l}}; \quad \xi_c = \frac{K_D k_0\omega_0^2}{2\omega_c}; \quad \text{and} \quad \omega_c^2 = k_s(\frac{1}{J_m^*}+\frac{1}{J_l}); \tag{13}$$

with

$$J_m^* = \frac{N^2 J_m}{K_P+1}. \tag{14}$$

The transfer function associated with the closed-loop system is similar to that of the open-loop. However, the link is now driven by a "motor," whose inertia is K_P+1 times smaller. Disturbance torques are also K_P+1 times smaller. A mechanical equivalent to the closed-loop system is shown in Figure 5, where J_m^* is the equivalent motor inertia. Given that $J_l \gg J_m^*$, the closed-loop parameters can be approximated as

$$k_c \approx 1; \quad \text{and} \quad \omega_c^2 \approx \frac{k_s}{J_m^*} = k_s\frac{K_P+1}{N^2 J_m}. \tag{15}$$

With $K_D > 0$, equations (12), (13) and (14) show the closed-loop system to be stable for all gains $K_P > -1$. For gains between -1 and 0 disturbances are amplified. Thus, in

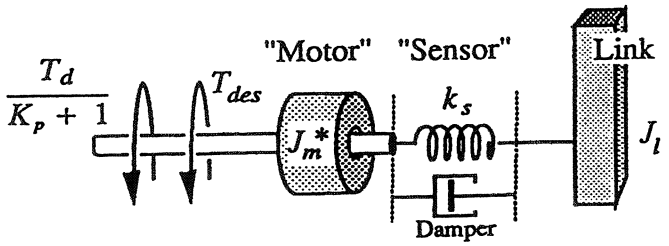

Figure 5: Closed-Loop System

order to achieve an improvement over the open-loop system, these gains must be larger than zero. This also means that the closed-loop frequency f_c must be larger than the open-loop frequency f_0.
Equation (15) provides a basis for trade-offs between achievable disturbance rejection $K_P + 1$, closed-loop bandwidth f_c, and sensor stiffness k_s. This equation (15) also shows that for a given achievable bandwidth, a lower sensor stiffness corresponds to a higher disturbance rejection, as observed by Whitney (1985) and Roberts (1985).

2.6 System Limitations

The closed-loop bandwidth, f_c, and the achievable gain, K_P, are limited by the following considerations:

- The sampling frequency of the digital controller must be at least five times higher than the closed-loop frequency f_c;
- The overall deadlag time in the measurements should not exceed a third of $1/f_c$;
- The first unmodeled resonant mode should be about three times higher then the closed-loop frequency;
- There are other limitations which result from noise in measurements and limit cycles due to backlash and nonlinear friction (Luh et al. 1983).

While a low sensor stiffness is desirable (equation 15) to achieve larger gains and better disturbance rejection, high gains result in increased motor activities. Higher motor torques will then be needed to counter the lower rigidity of the system. The transfer function of desired torque to motor torque is

$$NT_m = \frac{(K_P + 1)(s^2 + \omega_0^2)}{s^2 + 2\xi_c\omega_c s + \omega_c^2} T_{des}. \tag{16}$$

The Bode diagram of this transfer function (see Figure 6) shows that changes in the desired torque at frequencies higher than f_0 will require up to $K_P + 1$ times higher actuator torques. Below f_0 the required actuator torques are comparable to those needed for a rigid link.

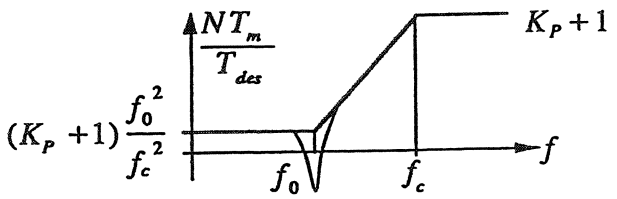

Figure 6: Required Motor Torque

PUMA Link

The limiting factor for the bandwidth in the PUMA link experiment has been the sampling frequency. Computer hardware has allowed a maximum sampling frequency of 500 Hz. The achievable closed-loop frequency can be estimated at $f_c = 100$ Hz which corresponds to a gain, K_P, of 19 (equation 15). This results in a 95% reduction of the effective friction $(1 - \frac{1}{K_P+1})$. In the actual experiment a factor of 97% has been achieved with a second order digital controller.
Torque changes with frequencies above the open-loop frequency (22 Hz for the fixed link and 41 Hz for the free link) require motor torques with very high amplitudes (up to 20 times (K_P+1) the desired torque). In practice, desired torques are much below the open-loop frequency. Under a lead-type controller, the high geared PUMA $(N^2 J_m/J_l = 2.5)$ becomes equivalent to a low geared manipulator with $J_m^*/J_l = 0.13$.

ARTISAN Link Prototype

For a low geared robot $(N^2 J_m \ll J_l)$, the achievable disturbance rejection $K_P + 1$ can be estimated as

$$K_P + 1 \approx (\frac{f_c}{f_0})^2. \tag{17}$$

The open-loop frequency of the link prototype is 230 Hz. A reduction factor of 95% of the effective friction corresponds to a closed-loop frequency around 1000 Hz. This is clearly much too high, considering the bandwidth limitations discussed above.

2.7 Lag Controller

When the dynamics of the open-loop system are too fast to be effectively controlled, one alternative is to ignore the high frequency of the open-loop system and to design a controller operating at lower frequency. The open-loop transfer function can then be approximated by

$$(k_s \to \infty) \quad T_s \approx k_0(NT_m + T_d). \tag{18}$$

Clearly, a lag controller is the most suitable for this zero-order system. A simple integral controller (see Figure 7) is selected for the following investigation of bandwidth limitations and disturbance rejection with lag-type controllers. The control law is

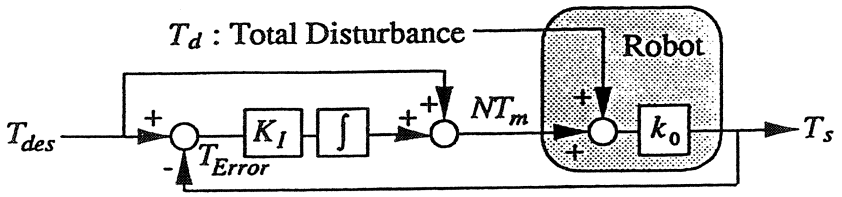

Figure 7: Integral Controller

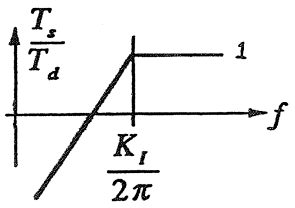

Figure 8: Disturbance Rejection

$$NT_m = T_{des} - K_I \int (T_s - T_{des})dt; \tag{19}$$

where K_I is the integral gain. The closed-loop transfer function can be obtained from equations (18) and (19) as

$$T_s = \frac{k_0(s + K_I)}{s + k_0 K_I} T_{des} + \frac{k_0 s}{s + k_0 K_I} T_d. \tag{20}$$

For low geared manipulators ($N^2 J_m \ll J_l$) the transfer function can be simplified to

$$T_s \approx T_{des} + \frac{s}{s + K_I} T_d. \tag{21}$$

With the above controller, disturbances are reduced for frequencies below $K_I/2\pi$ (see Figure 8). This type of controller is independent of the stiffness of the sensor. The achievable disturbance rejection will only depend on bandwidth limitations as described above. The behavior of the closed-loop system is similar to that of a direct drive manipulator ($T_s \approx T_{des}$).

2.8 Experimental Results

Figure 9 shows different step responses for the prototype link. The same digital controller with an overall lag characteristic was used to control the free link and the constrained link. The schematic of the controller is given in Figure 10.
The ARTISAN prototype has little natural damping and its open-loop bandwidth is 230 Hz as shown in Figure 9.a. The disturbance rejection bandwidth, $K_I/2\pi$, is 30 Hz. The 10-90% rise time for the closed-loop system (see Figure 9.b) is less than 10ms. Desired torque inputs, which are typically below the 30 Hz disturbance rejection bandwidth, are accurately controlled. A second order low-pass filter (150 Hz, $\xi = 1$) for the input is used to prevent the command torque from exiting the first resonant mode of 230 Hz.

In the case where the link is free (see Figures 9.c and 9.d), the resonant mode is excited by cogging in the transmission system. While the controller is unable to prevent this behavior, it provides a significant reduction of overshoot and static errors.

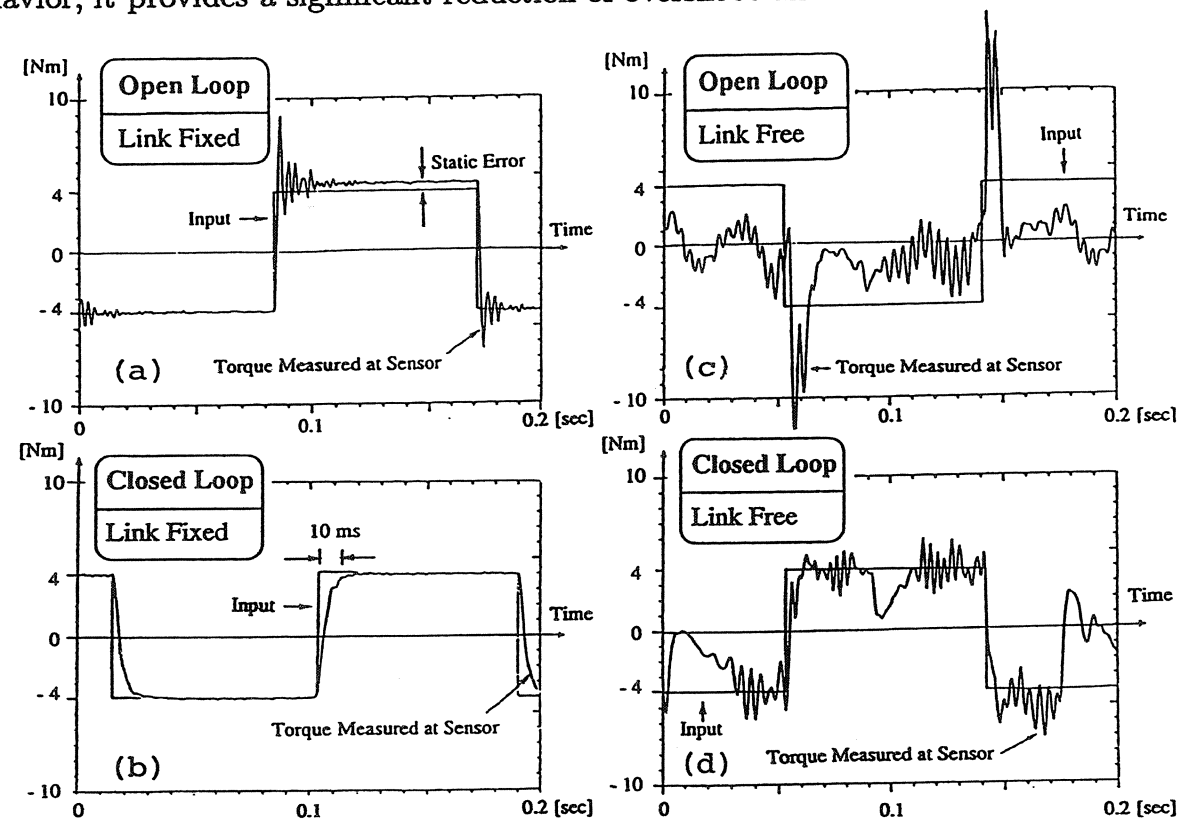

Figure 9: Prototype Step Responses

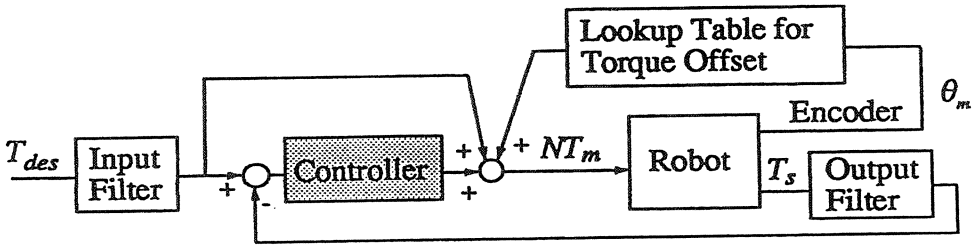

Figure 10: Controller Schematic

3 New Torque Sensor Design

Breakaway friction for manipulators with brush type servo-motors, e.g. the PUMA, is much higher (one order of magnitude) than the friction resulting from brushless motors. To bring about a reduction of the already low friction, high torque accuracy is needed for manipulators with brushless motors. For instance, the resolution needed (torque accuracy to maximum torque) for the sensor used in the prototype link has been

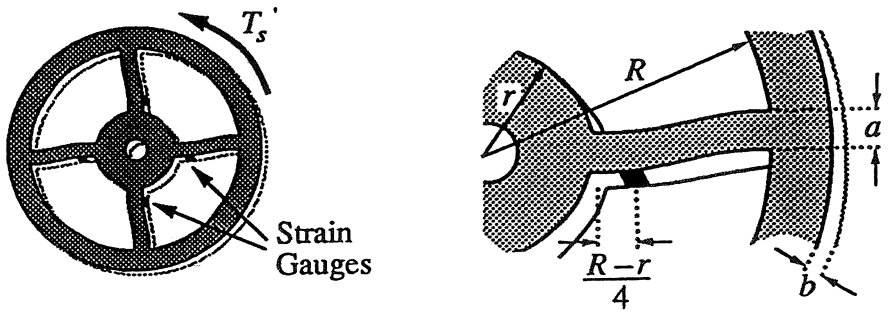

Figure 11: Strain Gauge Sensor

estimated at 0.03%. Building a sensor with such a resolution, in practice, is not an easy task.

3.1 Strain Gauge Sensors

As a first attempt at torque sensing, we have used the four beam torque sensor shown in Figure 11. Beam deflection is measured by semiconductor strain gauges. The torsional stiffness k_s' and the strain ϵ at the gauge location can be found as

$$k_s' = \frac{4Ea^3b(R^2+Rr+r^2)}{3(R-r)^3}; \quad \text{and} \quad \epsilon = \frac{3(R-r)(5R+r)}{16Ea^2b(R^2+Rr+r^2)}T_s'; \tag{22}$$

where E is the Young's modulus. Eight strain gauges arranged in Wheatstone bridges were used for each of the two sensors integrated in the two gears.
With this type of sensors, gear eccentricities have been shown to result in a position-dependent torque offset, which was 5 to 10 times higher than the required accuracy. The use of lookup tables to compensate for this dependency resulted in significant improvements but did not allow us to obtain the required resolution of 0.03%.

3.2 Sensor Placement

In the initial design of the prototype link, the sensor was placed in the gear as shown in Figure 12.a. With this arrangement, the sensor is not sensitive to those dynamic forces acting on the link, which do not contribute to the joint torque. At that location, however, the sensor is exposed to large radial forces caused by the transmission system. We have found and experimentally verified that very small eccentricities in the gear (10^{-5} to 10^{-6} meters) could result in radial forces high enough to saturate (and sometimes break) the strain gauges.
An alternative to this initial design (Figure 12.a) is shown in Figure 12.b. In this configuration the sensors are exposed to dynamic forces that do not contribute to the joint torque but are protected from the much larger radial forces due to eccentricities of the gear.
This second design was used for the new prototype. Further improvements in sensor disturbance protection can be achieved by using the configuration shown in Figure 12.c.

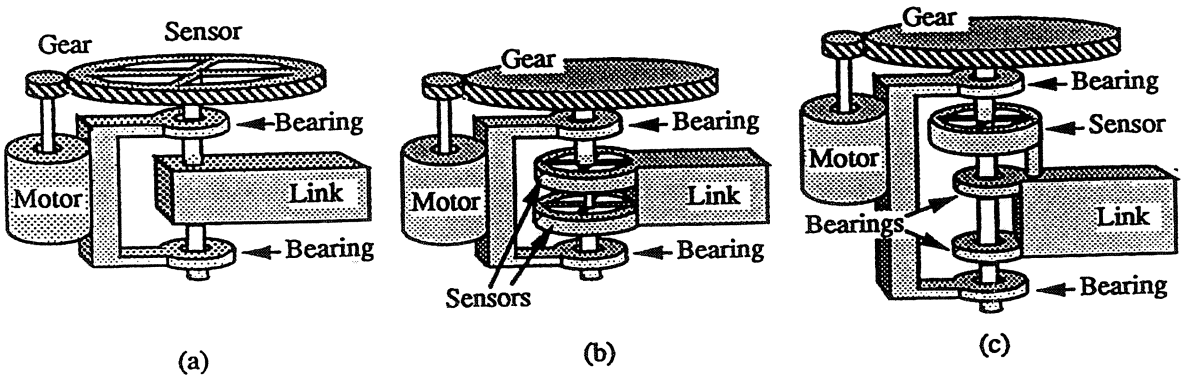

Figure 12: Sensor Placement

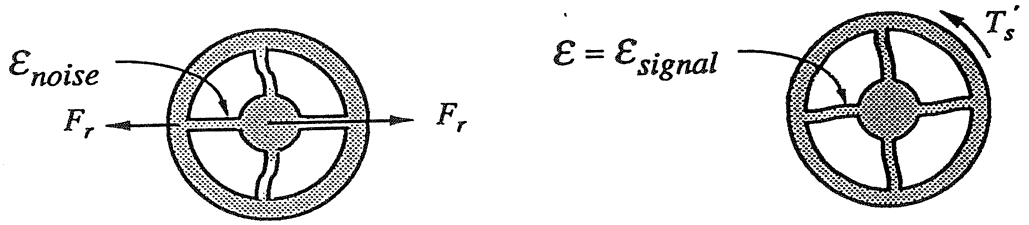

Figure 13: Signal-to-Noise Ratio

A second set of bearings is used to better protect the sensor from disturbances. Although significant improvements can be obtained by careful sensor design, radial forces cannot entirely be suppressed.

3.3 Modeling of Radial Forces

The effect of radial forces acting on each individual gauge can be formulated as a mechanical signal-to-noise ratio as shown in Figure 13.

The strain ε_{noise} caused by the radial force F_r depends on the direction of F_r. It can be shown that ε_{noise} reaches its maximum when F_r is parallel to the beam. The minimal signal-to-noise ratio (worst case) can be calculated as

$$\frac{\varepsilon_{signal}}{\varepsilon_{noise}} = \gamma \frac{T_s'}{F_r}\ ; \quad \text{with} \quad \gamma = \frac{3(5R+r)(R^2-2Rr+r^2+a^2)}{8a(R-r)(R^2+Rr+r^2)}. \tag{23}$$

The factor γ depends only on the geometry of the sensor. Since a 10 to 20 times increase of γ would provide the needed accuracy, we focused our effort on designs that would maximize the value of γ. We have also analyzed the signal-to-noise ratio characteristics for other sensor configurations, as shown in Figure 14.

Figure 14.a shows a torsional sensor as describe by Wu and Paul (1980). Those sensors have high robustness to radial forces, but are quite sensitive to torque disturbances in other directions. Figure 14.b shows an eight beam sensor. Although the addition of beams improves the signal-to-noise ratio, the manufacturing difficulty and sensor cost rapidly increase.

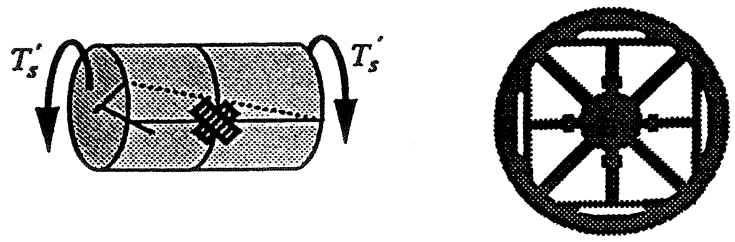

Figure 14: Torque Sensor Designs

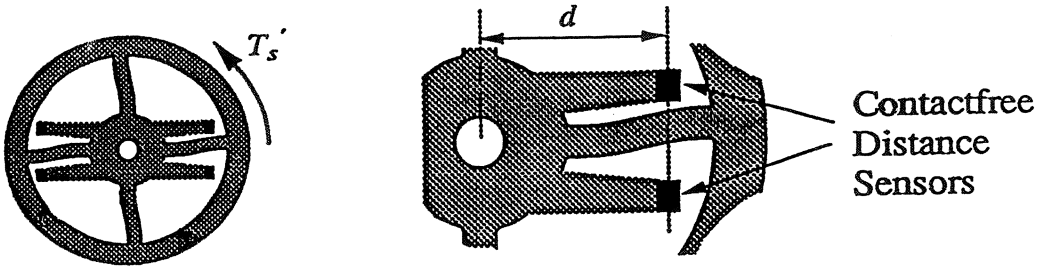

Figure 15: New Torque Sensor

3.4 New Torque Sensor

The design concept of the new sensor is illustrated in Figure 15. Torques are obtained from measurements of the beam deflections using four contact-free distance sensors. The deflection at the sensor location can be evaluated as

$$\Delta x = \Delta x_{signal} = d \frac{T_s'}{k_s'}. \tag{24}$$

A radial force, F_r, will result in a deflection $\Delta x = \Delta x_{noise}$, which depends on the direction of F_r. Δx_{noise} reaches its maximum when F_r is parallel to the measured deflection. The minimal signal-to-noise ratio (worst case) is

$$\frac{\Delta x_{signal}}{\Delta x_{noise}} = \gamma \frac{T_s'}{F_r}; \quad \text{with} \quad \gamma = \frac{3d(R^2 - 2Rr + r^2 + a^2)}{2a^2(R^2 + Rr + r^2)}. \tag{25}$$

A comparison of equations (23) and (25) clearly shows the advantages of the contact-free sensor over strain gauge based sensing.
The final layout of the new sensor is shown in Figure 16 and uses a six beam structure. Four inductive transducers are arranged in a Wheatstone bridge configuration. The signal-to-noise ratio of the new sensor is 24 times higher than the value obtained with the initial sensor ($\gamma = 1730\ \mathrm{m}^{-1}$).

3.5 Mechanical Robustness and Electrical Noise

The signal-to-noise ratio described above is an important parameter in the design of a torque sensor. However, the new torque sensor has other advantages, which for some applications might be more useful than its high resolution.

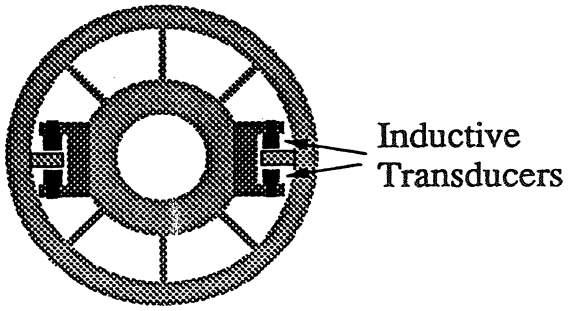

Figure 16: Torque Sensor Layout

Strain gauges are quite fragile and tend to break easily. Their maximum allowable strain is also fairly close to the strain at which they break, making failure prevention difficult. The inductive sensors are housed in steel cases and can withstand torques that are at least one order of magnitude higher than the maximum measurable torque.

Inductive sensors are also easy to mount and easily replaced, whereas mounting strain gauges (especially semiconductor ones) involves a lengthy procedure that requires expertise. Another shortcoming of strain gauges is their sensitivity to electrical noise. Their resolution (ratio of minimal to maximal measurable strain) is very high (up to 0.003% for semiconductors) but this accuracy can only be reached in an environment free of noise. With the new sensor, the inductive bridge is modulated with a carrier frequency of 5 kHz, which significantly reduces the sensitivity to electrical noise.

3.6 Conclusion

The issue of joint torque feedback has been discussed in the context of two manipulators with very different characteristics. The PUMA 560 is a high gear-ratio manipulator with a low open-loop resonant frequency, a characteristic which was shown to be compatible with a lead-type joint torque controller. For the low gear-ratio prototype link with high open-loop resonant frequency, a lag-type controller was used, resulting in a closed-loop behavior similar to that of a direct-drive system. These two controllers represent the two extremes in a wide spectrum of possible lead-lag controllers.

This paper also presented the design concept of a new type of torque sensor based on contactless distance measurements using inductive transducers. The signal-to-noise ratio achieved with the new sensor has been shown to be 24 times higher than the ratio obtained with conventional strain gauge sensors.

In addition to the conclusive results on the impact of joint torque feedback, these experiments have resulted in a better understanding of many theoretical and practical issues associated with the design and control of actuator/transmission systems using joint torque sensory feedback.

Acknowledgments

The financial support of SIMA, the Swiss NSF, and DARPA (contract DAAA21-89-C0002) are acknowledged. We are thankful to Professors Bernard Roth and Kenneth Waldron and to Richard Voyles, Larry Pfeffer and David Williams, who have made valuable contributions to the development of this work.

4 References

Armstrong, B., "Dynamics for Robot Control: Friction Modeling and Ensuring Excitation during Parameter Identification," Ph.D thesis, Department of Electrical Engineering, Stanford University, Stanford, CA, June 1988.

Asada, H., Youcef-Toumi, K., and Lim, S.K., "Joint Torque Measurement of a Direct Drive Arm," 23d IEEE Conference on Decision and Control, December 1984, pp. 1332-1337.

Colgate, E., and Hogan, N., "An Analysis of Contact Instability in Terms of Passive Physical Environments," Proc. IEEE International Conference on Robotics and Automation, Scottsdale, Arizona, 1989, pp. 404-409.

Eppinger S.D., and Seering W. P., "On Dynamics of Robot Force Control," Proc. IEEE International Conference on Robotics and Automation, San Francisco, CA, 1986.

Eppinger, S.D., and Seering, W. P., "Understanding Bandwidth Limitations in Robot Force Control," Proc. 1987 IEEE International Conference on Robotics and Automation, Raleigh, N.C., CA, April 1987.

Khatib, O., Burdick, J., "Motion and Force Control of Robot Manipulators," Proc. International Conference on Robotics and Automation, San Francisco, CA, April 1986, pp. 1381-1386.

Luh, J.Y.S., Fisher, W.D., and Paul, R.P., "Joint Torque Control by a Direct Feedback for Industrial Robots," IEEE Transactions on Automatic Control, AC-28, 1983, pp. 153-160.

Pfeffer, L., Khatib, O., and Hake, J., "Joint Torque Sensory Feedback in the Control of a PUMA Manipulator," Proc. American Control Conference, Seattle, Washington, June 1986, pp. 818-824.

Roberts, R.K. Paul, R.P., and Hillberry, B.M., "The Effect of Wrist Sensor Stiffness on the Control of Robot Manipulators," Proc. IEEE International Conference on Robotics and Automation, St. Louis, MO, March 1985, pp. 269-274.

Roth, B., Raghavan, M., Khatib, O., and Waldron, K., "Kinematic Structure for a Force Controlled Redundant Manipulator," Proc. International Meeting on Advances in Robot Kinematics, Ljubljana, Yugoslavia, September 1988, pp. 62-66.

Townsend, W., "The Effect of Transmission Design on Force-Controlled Manipulator Performance," Ph.D thesis, Artificial Intelligence Laboratory, Massachusetts Institute of Technology, Cambridge, MA, 1988.

Whitney, D.E., "Historical Perspective and State of the Art in Robot Force Control," Proc. IEEE International Conference on Robotics and Automation, St. Louis, MO, March 1985, pp. 883-889.

Wu, C.H., and Paul, R.P., "Manipulator Compliance Based on Joint Torque Control," 19th IEEE Conference on Decision and Control, December 1980, pp. 88-94.